*Turkish Journal of Civil Engineering, 2027, xxxx-xxxx, Paper xxx,* ***Research Article***

# Novel Lightweight Artificial Aggregate Production: 3D-Printed Aggregate in Lightweight Concrete

**Tarik OMUR**[1*]

## ABSTRACT

This study introduces a novel lightweight artificial aggregate manufactured using fused deposition modeling (FDM) 3D-printing and evaluates its influence on the fresh, mechanical, physical, and durability performance of lightweight aggregate concrete (LWAC). Three aggregate geometries, spherical, edged, and irregular were fabricated from polylactic acid (PLA), and the optimal printing infill density was determined through a multi-criteria decision-making approach using TOPSIS, considering particle crushing strength (PCS), density, and production cost. The optimized 100% infill density configuration was subsequently employed in LWAC mixtures, in which 3D-printed aggregates fully replaced natural pumice aggregate. The results demonstrate substantial performance improvements across all mixtures incorporating 3D-printed aggregates (3DPA). The 28-day compressive strength of concrete increased by 15-34% relative to pumice-based LWAC, while all mixtures achieved a density lower than 2000 kg/m$^3$. The water absorption and open porosity decreased by up to 32% and 27%, respectively, owing to the impermeable polymeric shell of the 3DPA. Capillary sorptivity significantly reduced for spherical and edged geometries, while irregular shapes induced slightly higher sorptivity due to geometry-related ITZ heterogeneities. The abrasion resistance improved by as much as 23%, and chloride migration resistance exhibited remarkable enhancement, with spherical and edged aggregate concretes yielding “very low” $D_{nssm}$ values (<5×10$^{-12}$ m$^2$/s). Overall, the findings highlight the potential of additive-manufactured artificial aggregates as a tunable, high-performance alternative to natural lightweight aggregates like pumice, enabling durability-enhanced LWAC production with superior mechanical and physical performance.

**Keywords:** Fused Deposition Modeling (FDM), lightweight artifical aggregate, pumice, 3D-printing, TOPSIS.

---

Note:
- This paper was received on March 31, 2026 and accepted for publication by the Editorial Board on July 16, 2026.
- Discussions on this paper will be accepted by xxxxxxx xx, xxxx.

- https://doi.org/

1 Yildiz Technical University, Department of Civil Engineering, Istanbul, Türkiye
tomur@yildiz.edu.tr - https://orcid.org/0000-0002-1488-5028

* Corresponding author

## 1. INTRODUCTION

Lightweight aggregate concrete (LWAC) has become a versatile and essential material in contemporary civil engineering, driven by the growing demand for sustainable, structurally efficient, and high-performance infrastructure systems [1,2]. The replacement of conventional normal-weight aggregates with lightweight aggregates (LWAs) leads to a substantial reduction in the overall density and self-weight of concrete elements [3]. This marked reduction in dead load not only decreases transportation and handling demands but also facilitates the optimization of structural design and the development of more efficient construction systems [4]. In addition to reducing structural load, LWAs enhance the thermal insulation capacity and seismic resilience of concrete, thereby reinforcing the significance of LWAC in modern civil engineering applications [2].

Natural LWAs such as pumice, volcanic tuff, and diatomite have long been employed in construction to decrease the self-weight of concrete elements while simultaneously improving their thermal insulation performance [5]. These naturally occurring porous materials offer intrinsic benefits, such as low density and superior thermal properties, while requiring no energy-intensive or intricate manufacturing processes [6]. However, the structural application of natural LWAs like pumice is significantly hindered by their highly porous and heterogeneous microstructures, which inherently result in excessively high and variable water absorption capacities alongside lower mechanical strengths [6]. Moreover, the inherently irregular morphology of these traditional aggregates limits precise geometric control, thereby constraining the optimization of particle packing and the achievable porosity spectrum, while the large-scale extraction of such materials contributes significantly to environmental degradation, land disturbance, and the depletion of natural resources [7,8]. In contrast, artificial lightweight aggregates (ALWAs) derived from industrial by-products or pelletizing present a highly sustainable and customizable alternative to natural resources [9,10]. Unlike their natural counterparts, ALWAs offer the distinct advantage of tailored physical and mechanical properties, allowing for precise control over aggregate size, shape, and porosity. This morphological and microstructural control ultimately yields competitive load-bearing capabilities and consistent moisture dynamics, making ALWAs superior candidates for modern, eco-efficient structural applications.

Beyond the topological and physicomechanical attributes of natural LWAs and ALWAs, the morphological characteristics of aggregates, whether spherical, angular, or irregular play a decisive role in governing both the fresh and hardened properties of LWAC. Numerous studies have shown that spherical and well-rounded LWAs substantially enhance fluidity by reducing interparticle friction, whereas highly angular and irregular particles tend to impede flowability. In the hardened state, aggregate morphology also exerts a critical influence on the quality of the interfacial transition zone (ITZ) and the extent of mechanical interlocking [11–13]. Therefore, the particle morphology of LWAs is a critical parameter influencing both fresh and hardened performance of LWAC. In this context, ALWAs provide notable advantages over natural LWAs, as their particle size and shape can be precisely engineered to achieve desired performance outcomes.

To address the intrinsic limitations and natural variability associated with conventional LWAs such as pumice, perlite, and vermiculite, there has been a pronounced shift toward the development of engineered artificial aggregates. Natural LWAs are inherently constrained by their geological origin, which leads to highly inconsistent porosity, unpredictable mechanical strength, and excessive water absorption, often necessitating pretreatment techniques such as extended presoaking [14,15]. These variabilities complicate mix design and undermine the reliability of both fresh and hardened concrete properties. Although traditional artificial aggregates, including expanded clay and sintered fly ash, offer improved consistency, they still lack the capacity for precise and repeatable control over individual particle morphology [1]. Hence, advanced manufacturing technologies like 3D-printing could be a transformative platform for artificial aggregate production. By transitioning from conventional bulk processing to precision-based fabrication, it becomes possible to engineer artificial aggregates with tightly controlled geometrical and microstructural characteristics, effectively eliminating the stochastic nature of traditional materials and enabling the creation of highly tailored, application-specific solutions. To date, the use of 3D-printing and similar advanced technologies in the context of concrete aggregates has rarely been investigated via four distinct approaches. The first is indirect printing, in which 3D-printed molds or master patterns are employed to cast cement or mineral-based aggregates with controlled geometry. This strategy has been used to fabricate standardized pavement coarse aggregates and high-precision morphological reference materials, but the resulting aggregates remain conventional cementitious materials and the polymer serves only as a sacrificial mold [16,17]. The second comprises model polymer aggregates produced by injection molding or printing for fundamental investigations of particle shape on packing porosity, tortuosity, and permeability, typically in unbound configurations and combined with discrete-element modelling, rather than as functional aggregates within hardened concrete [8]. The third is extrusion-based 3D concrete printing incorporating coarse aggregate, in which the focus is the printability and directional mechanical behaviour of the printed cementitious element itself, not the manufacture of the aggregate [18]. The fourth involves 3D-printed polymer reinforcement, such as printed trusses, shells, or bar replacements embedded in concrete, where the printed polymer acts as reinforcement rather than as aggregate [19].

In contrast to all the above, the present study directly fabricates the LWAs itself from polylactic acid (PLA) via fused deposition modeling (FDM) 3D-printing technology and employs it as a complete replacement for natural pumice in LWAC production. This approach is distinguished by four features that, to the best of the authors' knowledge, have not previously been combined: (i) the aggregate is an additively manufactured polymeric particle rather than a cast cementitious body or a sacrificial mold; (ii) particle geometry (spherical, edged, irregular) and internal porosity (infill density) are decoupled and independently controlled, enabling isolation of the geometry effect; (iii) the internal structure of 3D-printed aggregates (3DPAs) is optimized through the multi-criteria decision-making (TOPSIS and VIKOR) frameworks balancing particle strength, density, and cost; and (iv) the resulting LWACs are comprehensively characterized across fresh, mechanical, physical (absorption and sorptivity), and durability (abrasion and chloride migration resistance) performance. This establishes a new framework for integrating additive manufacturing into the design of engineered LWAs.

## 2. MATERIALS AND METHODOLOGY

### 2.1. Raw Materials

The commercially available CEM I 42.5 R grade portland cement (PC) with a specific gravity of 3.10 was used as the primary binding material for the preparation of LWACs. The oxide composition of PC is tabulated in **Table 1**. The corresponding mineralogical phase composition indicated proportions of 68.85% alite, 1.67% belite, 6.41% aluminate, and 9.60% ferrite. The particle size distribution (PSD) curve of PC is shown in **Figure 1**.

*Table 1 - The chemical composition of PC*

| Oxide composition (%) | $SiO_2$ | $Al_2O_3$ | $Fe_2O_3$ | CaO | MgO | $SO_3$ | $K_2O$ | $Na_2O$ | LOI* |
|---|---|---|---|---|---|---|---|---|---|
| PC | 18.67 | 4.43 | 3.16 | 63.92 | 1.06 | 3.47 | 0.9 | 0.13 | 3.95 |

*: Loss on ignition

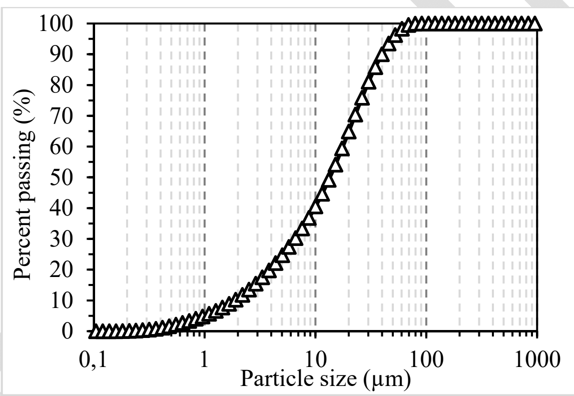


*Figure 1 - The particle size distribution of PC.*

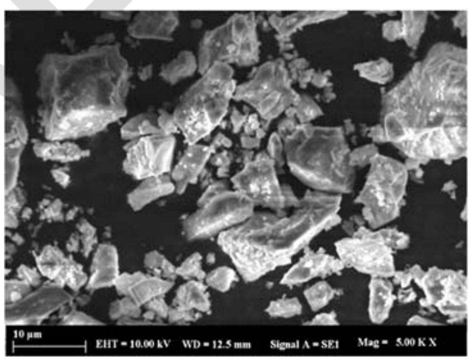


*Figure 2 - SEM image of PC.*

The $D_{10}$, $D_{50}$, and $D_{90}$ values of PC were found as 1.9 µm, 13.5 µm, and 39.8 µm, respectively. **Figure 2** illustrates the scanning electron microscopy (SEM) image of PC particles. The SEM observations revealed that the PC particles predominantly exhibit angular morphologies. A commercially available polycarboxylate ether-based superplasticizer with a density of 1.1 kg/L was incorporated to ensure the desired flowability of the concrete mixtures. Tap water was utilized as the mixing water throughout the preparation process.

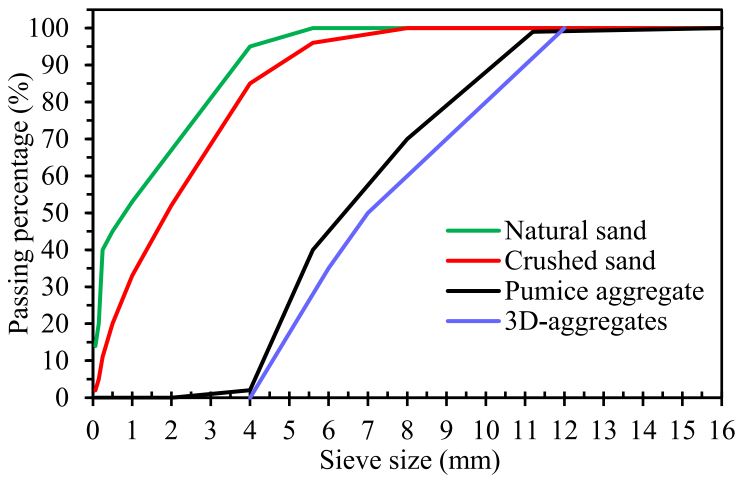


*Figure 3 - The sieve analysis results of aggregates*

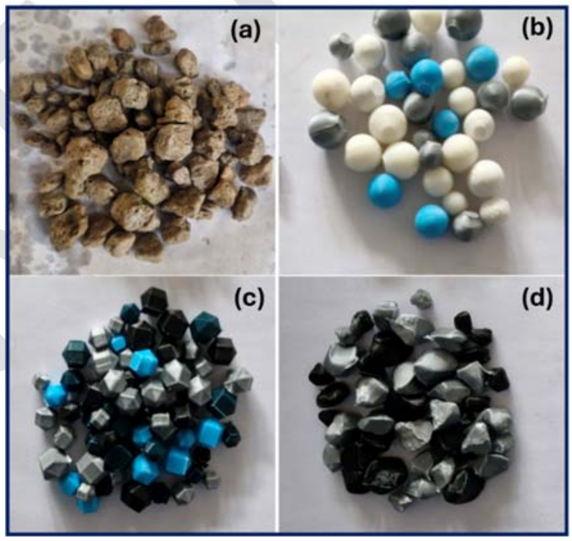


*Figure 4 - Visual representations of: (a) pumice aggregates, (b) spherical 3D-printed artificial aggregates, (c) edged 3D-printed artificial aggregates, and (d) irregular-shaped 3D-printed artificial aggregates.*

During the production of the LWAC mixtures, natural siliceous sand and crushed sand were employed as fine aggregates. The particle densities of the natural and crushed sands were measured as 2.63 g/cm$^3$ and 2.69 g/cm$^3$, respectively. For the coarse aggregate fraction, two distinct lightweight aggregate types were utilized: (i) natural pumice aggregate (NPA) and (ii) 3DPA. The PSD curves of the fine and coarse aggregates are presented in **Figure 3**.

According to TS EN 1097 [20], the NPA exhibited an oven-dry density of 593 kg/m$^3$, porosity of 73%, and a water absorption capacity of 49%. The physical appearances of aggregates are illustrated in **Figure 4**. As shown in this figure, 3DPAs with the similar particle size distribution and $D_{max}$ value (11.2 mm) as NPAs were produced in three distinct geometries. It is noteworthy that the NPAs were pre-soaked in water for 24 h prior to concrete mixing to minimize undesired absorption of the mixing water during batching. The details regarding the properties and production of 3DPAs are provided in **Section 2.2**.

### 2.2. Production of 3D-Printed Artificial Aggregates

The lightweight artificial aggregates were fabricated using an FDM-based 3D-printing process. Polylactic acid (PLA), a recyclable thermoplastic polyester, served as the primary feedstock for aggregate production. The overall manufacturing workflow is depicted in **Figure 5**. Initially, two distinct aggregate geometries (spherical and edged) were designed using an open-source CAD software of Tinkercad. In addition, the irregular-shaped aggregates were generated using a photogrammetry-based reconstruction workflow to replicate the morphology of natural crushed-stone particles. One hundred randomly selected crushed-stone particles ($D_{max}$ = 11.2 mm) were imaged using a 48 MP fusion main camera with a quad-pixel system, and three-dimensional surface models were reconstructed in an open software of Meshroom v.2025.1.0. The resultant meshes were refined and rendered using the open-source mesh-processing tools of Blender v.5.1 software, exported as STL files, and later processed in Bambu Studio slicing software for print-path generation. The printing process was performed using a monotonic-linear infill pattern with a layer height of 0.2 mm and two wall loops. The adopted linear infill pattern (illustrated in **Figure 6** alongside other common patterns) is a rectilinear-type pattern in which successive infill lines are deposited consistently in a single direction, rather than in alternating directions. This unidirectional path planning yields a homogeneous and gap-free internal structure with highly uniform line spacing [21]. This pattern was selected deliberately since the present study requires that nominally identical aggregates exhibit consistent particle density and crushing strength, a prerequisite for both the reliability of the optimization and the controlled isolation of particle-geometry effects. Thus, the reproducibility and density uniformity were ranked over the maximization of any single mechanical property [22]. The infill density of the artificial aggregates was then optimized through the Technique for Order Preference by Similarity to Ideal Solution (TOPSIS) multi-criteria decision-making method, considering particle crushing strength (PCS), particle density, and printing cost, as detailed in **Section 3.1**. The infill density denotes the percentage of the internal volume of the printed aggregate particle that is occupied by deposited material, where the remainder being air voids. It is controlled by the spacing of the internal infill lines in this selected monotonic infill pattern. A 0% infill corresponds to a hollow particle bounded only by the perimeter walls, whereas a 100% infill yields a fully solid particle. As illustrated in **Figure 6b**, increasing the infill density reduces the spacing between the deposited lines and progressively raises the particle density, thereby governing both the mass and the crushing strength of the aggregate.

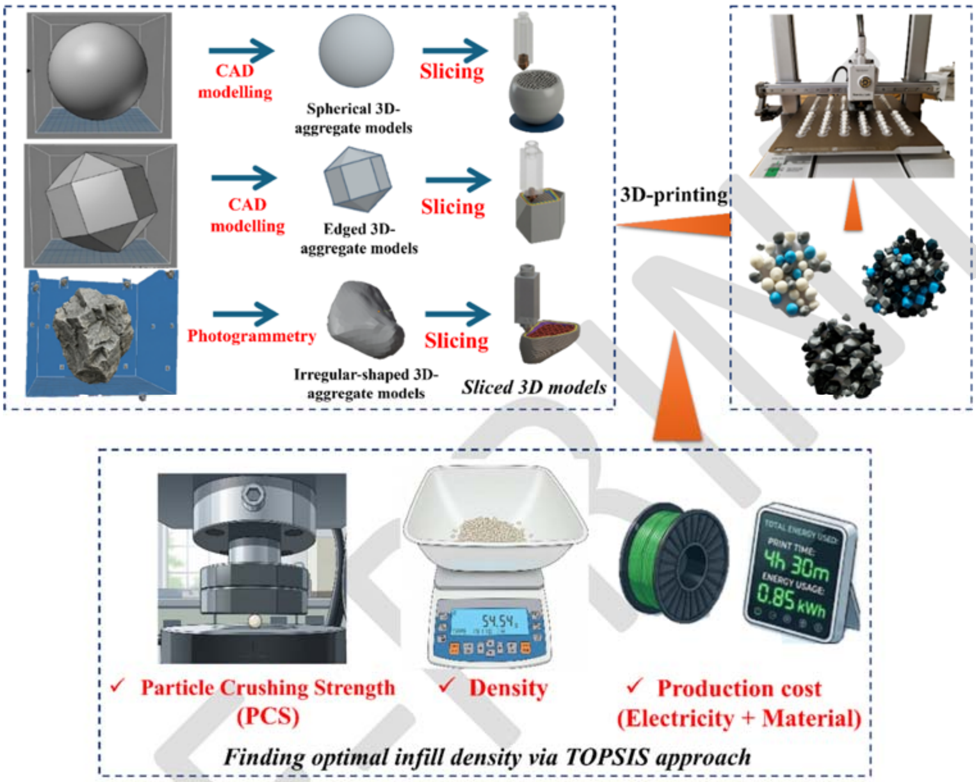


*Figure 5 - The schematic illustration of the production and characterization of 3D-printed artificial aggregates*

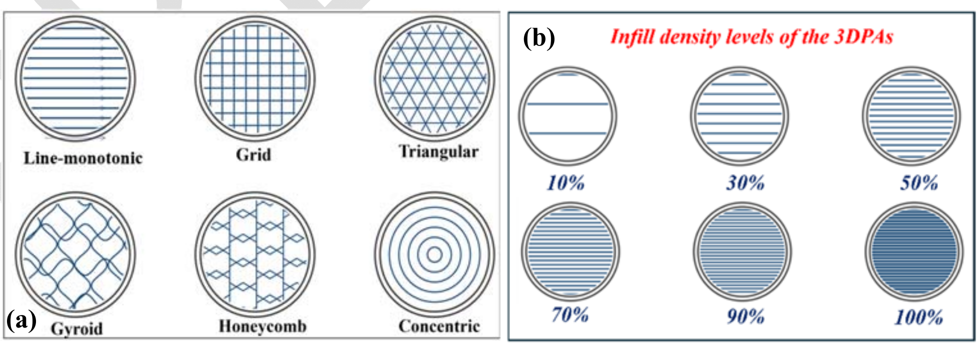


*Figure 6 – The representation of: (a) common FDM infill patterns and (b) various infill density levels shown on a spherical aggregate cross-section*

### 2.3. Mix Design and Sample Preparation

**Table 2** presents the mix design parameters adopted for the production of LWAC specimens. Four concrete mixtures were prepared to evaluate the influence of different 3D-printed aggregate geometries on the performance of LWAC. A pumice-based mixture served as the reference, and in the remaining mixtures, the pumice coarse aggregate was fully replaced with 3D-printed aggregates of spherical, edged, and irregular shapes, respectively. As outlined in **Table 2**, all other mixture design variables, including cement content, water-to-cement (w/c) ratio, aggregate-to-concrete volume fraction, fine-to-coarse aggregate proportion, and superplasticizer dosage (by weight of cement), were kept constant across the mixes. The nomenclature of the mixtures reflects the geometry and type of coarse aggregate (NPA or 3DPA) employed; specifically, “PMC” denotes the NPA-based control mixture, while “SPH”, “EDG”, and “IRR” correspond to the mixtures incorporating spherical, edged, and irregular 3DPAs, respectively.

The preparation of the concrete specimens commenced with the homogenization of tap water and the pre-batched dry constituents in a mechanical mixer, where mixing was maintained for 5 min to ensure uniform dispersion. The resulting fresh LWAC mixture was subsequently placed into the designated molds in two layers, each compacted by vibration for about 5 s to eliminate entrapped air. After 24 h, the specimens were demolded and transferred to a curing environment consisting of lime-saturated water maintained at 22±2 °C.

*Table 2 - Mix design parameters of concrete mixes.*

| Mix code | PC ($kg/m^3$) | w/c ratio | Natural sand (vol. %) | Crushed sand (vol. %) | Pumice (vol. %) | 3D-artificial aggregate (vol. %) | Superplasticizer (wt. %) |
|---|---|---|---|---|---|---|---|
| PMC | 400 | 0.45 | 30 | 30 | 40 | - | 1.0 |
| SPH | 400 | 0.45 | 30 | 30 | - | 40 | 1.0 |
| EDG | 400 | 0.45 | 30 | 30 | - | 40 | 1.0 |
| IRR | 400 | 0.45 | 30 | 30 | - | 40 | 1.0 |

### 2.4. Experimental Schedule

#### *2.4.1. Artificial Aggregate Properties And Infill-Density Optimization*

The cost, particle density, and PCS of the spherical 3DPAs were evaluated to characterize and optimize their infill-density configuration. The production cost of the artificial aggregates was determined by combining the expenses associated with PLA filament consumption and the electrical energy required to fabricate each individual particle. The aggregate density was determined by relating each specimen’s measured mass to its corresponding geometric volume. PCS measurements were conducted using a uniaxial compression testing apparatus, as illustrated in **Figure 5**, wherein the aggregates were loaded vertically at a constant displacement rate of 0.5 mm/min until failure occurred, detailed in [23]. For each aggregate category, five particles were tested to establish representative PCS values, calculated in accordance with **Equation (1)**.

$$\sigma(MPa) = \frac{2.8\times P}{\pi\times d^2} \quad (1)$$

where, '$\sigma$' represents the PCS value in MPa, whereas '$P$' and '$d$' demonstrate the failure load in N and aggregate diameter in mm, respectively.

The spherical 3DPAs were produced in three nominal diameters, 8 mm, 12 mm, and 16 mm to evaluate the influence of infill-density on their physical and mechanical characteristics. For each diameter, aggregates were fabricated at eleven infill-density levels, ranging from 10% to 100% in 10% increments. For each aggregate batch, the PCS, particle density, and production cost were determined, as these parameters collectively represent the primary performance and economic indicators relevant to aggregate production. The obtained values were then incorporated into a multi-criteria decision-making framework based on TOPSIS. In TOPSIS procedure, PCS was defined as a beneficial attribute, whereas particle density and printing cost were treated as non-beneficial attributes. Each parameter set was normalized, weighted, and ranked according to its Euclidean distance to the positive and negative ideal solutions. The entropy weighting method was employed to quantitatively determine the relative importance of each evaluation criterion. The TOPSIS analysis was performed independently for each aggregate diameter, enabling the identification of the optimal infill-density value specific to the size category. This systematic multi-criteria approach ensured a balanced assessment of mechanical performance, lightweight characteristics, and fabrication efficiency, ultimately yielding an optimized infill-density selection for subsequent LWAC production.

#### 2.4.1.1. Weighting-Sensitivity Analysis of the TOPSIS Optimization

To confirm that the selected optimal infill density was robust and not dependent on a single weighting choice, the TOPSIS optimization was subjected to a three-part robustness check. First, to avoid reliance on subjectively assigned weights by entropy method, the criterion weights were also determined using the Criteria Importance Through Intercriteria Correlation (CRITIC) method, which derives weights solely from the statistical characteristics of the decision matrix [24]. Second, the rankings were independently reproduced using VlseKriterijumska Optimizacija I Kompromisno Resenje (VIKOR), an alternative multi-criteria decision-making method [25], to verify that the outcome was not specific to the TOPSIS algorithm. The agreement between the two rankings was also quantified using the Spearman rank correlation coefficient. Third, a continuous weight-sensitivity analysis was performed in which the weight assigned to PCS varied across its full range, while the remaining weight was shared equally between particle density and cost, thereby mapping the optimal configuration over the entire weight space rather than at discrete points.

In addition, to identify the configuration most appropriate for a lightweight-prioritized design objective, a constrained selection was applied in which particle density and cost were minimized subject to a minimum particle-strength requirement derived from existing studies. The procedural details of the entropy, CRITIC, and VIKOR methods are well established and are provided in the cited references.

### 2.4.2. *Concrete Testing*

#### 2.4.2.1. Flowability

The flowability of the fresh concrete mixtures was assessed using the mini-slump test in accordance with ASTM C1437 [26]. The flow spread of each mixture was measured along four predefined axes on the testing surface, and the resulting values were expressed as a percentage of the original base diameter of 10 cm.

#### 2.4.2.2. Compressive Strength

The compressive strength of three identical cubic concrete specimens with a dimension of 70×70×70 $mm^3$ was evaluated at 7 and 28 days. The selected sample dimension is approximately six times the maximum aggregate size ($D_{max}$ = 11.2 mm) and therefore exceeds the minimum specimen-to-aggregate dimensional ratio (≥3.5× $D_{max}$) required by EN 12390-1 [27], ensuring that the specimen size does not bias the measured strength. The hardened density was determined at 28 days from the mass and geometric dimensions of the same specimens, and the strength-to-density (specific strength) ratio was subsequently calculated.

#### 2.4.2.3. Physical and Transport Properties

The open porosity and water absorption of the concrete specimens were evaluated in accordance with the referenced procedure [28]. Initially, the samples were oven-dried at around 55±5 °C for 2 days until a constant mass ($M_{od}$) was achieved, after which they were placed in an airtight chamber. A reduced drying temperature of 55 °C was intentionally adopted for all specimens, in place of the conventional high-temperature oven-drying process, so as to prevent any thermal alteration of the PLA aggregate phase. Since the selected temperature remains well below the cold-crystallization temperature (90 °C) and melting temperature (160-180 °C), annealing or crystallization-induced changes to the PLA polymer can be considered as negligible [29]. After drying, a vacuum of 2 kPa was applied for two hours to evacuate air from the accessible pore network. The deionized water was then gradually introduced while maintaining the same vacuum pressure to ensure complete immersion of the specimens. Once submerged, the chamber was returned to atmospheric pressure, and the samples remained in water for 24 h. Subsequently, their saturated surface-dry mass ($M_{sa}$) and submerged mass ($M_{sw}$) were measured. The open porosity was then calculated using **Equation (2)**.

$$Open\ porosity\ (\%) = \frac{M_{sa}-M_{od}}{M_{sa}-M_{sw}} \times 100 \quad (2)$$

The sorptivity of the mortar specimens was assessed at 28 days following ASTM C1585 standard [30]. The concrete samples (100 mm in diameter and 50 mm in height) were first conditioned in a controlled-environment chamber operated at 50 °C and 80% relative humidity. After conditioning, the specimens were sealed in airtight containers for 15 days, and their lateral surfaces were coated with epoxy resin to eliminate side moisture ingress. The test commenced by placing each specimen in water with the water level maintained approximately 3 mm above the base. The mass gain of the specimens was monitored at designated intervals, and the initial and secondary sorptivity coefficients were determined as the average of two replicate concrete samples.

#### 2.4.2.4. Abrasion Resistance

The Böhme test was used to assess the abrasion resistance of three replicate LWAC specimens oven-dried at around 55±5 °C to constant mass in accordance with EN 1338 [31]. Each specimen underwent a total of 16 abrasion cycles, each comprising 22 revolutions, and the average mass and height losses were recorded at the end of each four cycle. In addition, the loss in volume of concrete after 16 cycles ($\Delta V$ ($mm^3$/50 $cm^2$)) was calculated using **Equation (3)**.

$$\Delta V = \frac{\Delta m}{\rho} \tag{3}$$

In this equation, "$\Delta m$" (g) and "$\rho$" ($g/mm^3$) denote the overall mass loss and density of specimens.

#### 2.4.2.5. Chloride Migration Resistance

The chloride migration resistance of concrete specimens was evaluated at 28 days in accordance with NT Build 492 [32]. The cylindrical discs (50 mm × 100 mm) were preconditioned by applying a 50-mbar vacuum for 3 h and subsequently immersing them in lime-saturated water for 18 h. The specimens were then mounted in the migration cell containing 10% NaCl catholyte and 0.3 N NaOH anolyte. An initial voltage of 30 V was applied to establish the required test duration from the measured current. After completion, each sample was split axially and 0.1 M $AgNO_3$ was sprayed on the split surface to reveal the chloride penetration front. The average penetration depth was recorded and used to calculate the non-steady-state migration coefficient ($D_{nssm}$).

## 3. RESULTS AND DISCUSSION

### 3.1. Characterization and Optimization of 3D-Printed Artificial Aggregate Production

The infill-density of 3D-printed components is a key parameter governing their mechanical performance and density. **Figure 7** shows the variation of PCS, particle density and unit cost values with the variation of infill density of artificial aggregates. Across the tested infill-density levels, the PCS values varied between 8.3 and 42.2 MPa for the 8 mm aggregates, 4.7 to 22.7 MPa for the 12 mm aggregates, and 4.4 to 24.1 MPa for the 16 mm aggregates. In contrast, particle density was less sensitive to aggregate size but increased from 0.46 to 1.17 $g/cm^3$ as the infill-density increased. The test results indicated that an increase in infill-density led to a systematic rise in the PCS, particle density, and unit production cost of the 3DPAs. Notably, for the 8 mm and 16 mm aggregates, the PCS values nearly doubled when the infill-density was raised from 70% to 100%, while the corresponding increase in cost remained relatively low. Additionally, depending on the aggregate size, the particle density exhibited an increase of approximately 15-27% over the same infill-density interval. Thus, TOPSIS results are depicted in **Table 3** and **Figure 8** to subjectively select the most appropriate infill-density of artificial aggregates. The TOPSIS analysis identified the 100% infill-density configuration as the most favorable option for all aggregate sizes. Conversely, aggregates produced with 10% and 20% infill levels ranked lowest in overall suitability. This outcome is consistent with the observation that fully solid aggregates delivered the highest PCS values, reaching up to 42.2 MPa despite their increased density and production cost. It is worth noting that the closeness coefficient ($G_i^*$) and the distance to the suitable solution ($S_i$) of TOPSIS were derived using the entropy-weighting approach, in which weights are assigned based on the dispersion of numerical responses rather than rank variation. It is emphasized that the analysis simultaneously considered three criteria, PCS (beneficial), particle density, and production cost (both non-beneficial). The entropy-weighting method assigns weights objectively according to the dispersion of each criterion; as PCS exhibited the greatest variability across infill levels, it received the highest weight. The dominance of the 100% configuration therefore reflects this data-driven weighting rather than an explicit prioritization of strength.

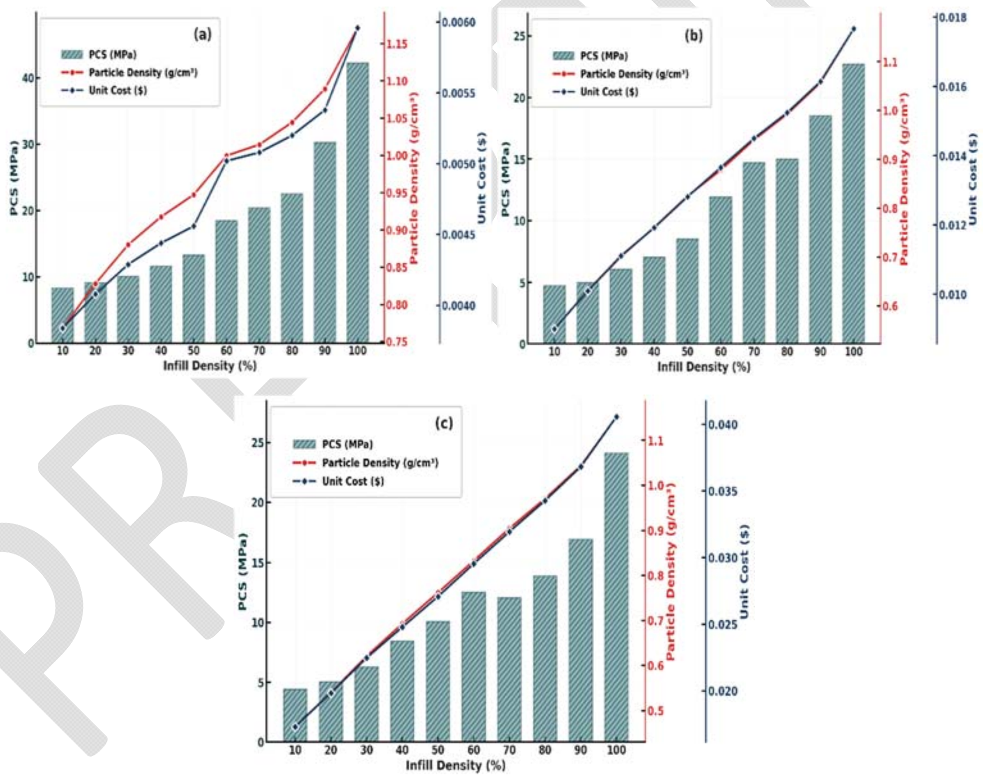


*Figure 7 - The properties of 3D-printed artificial aggregates: (a) 8 mm-diameter, (b) 12 mm-diameter, and (c) 16 mm-diameter*

*Table 3 - The closeness coefficient and the rank of infill-densities depending on particle diameter*

| Infill-density (%) | $G_i^*$ / Rank (8 mm) | $G_i^*$ / Rank (12 mm) | $G_i^*$ / Rank (16 mm) |
|---|---|---|---|
| 10 | 0.021 / 10 | 0.104 / 9 | 0.174 / 8 |
| 20 | 0.031 / 9 | 0.094 / 10 | 0.164 / 10 |
| 30 | 0.055 / 8 | 0.110 / 8 | 0.172 / 9 |
| 40 | 0.099 / 7 | 0.146 / 7 | 0.237 / 7 |
| 50 | 0.147 / 6 | 0.217 / 6 | 0.302 / 6 |
| 60 | 0.301 / 5 | 0.400 / 5 | 0.413 / 4 |
| 70 | 0.357 / 4 | 0.553 / 4 | 0.387 / 5 |
| 80 | 0.419 / 3 | 0.567 / 3 | 0.471 / 3 |
| 90 | 0.647 / 2 | 0.753 / 2 | 0.610 / 2 |
| 100 | 0.979 / 1 | 0.896 / 1 | 0.826 / 1 |

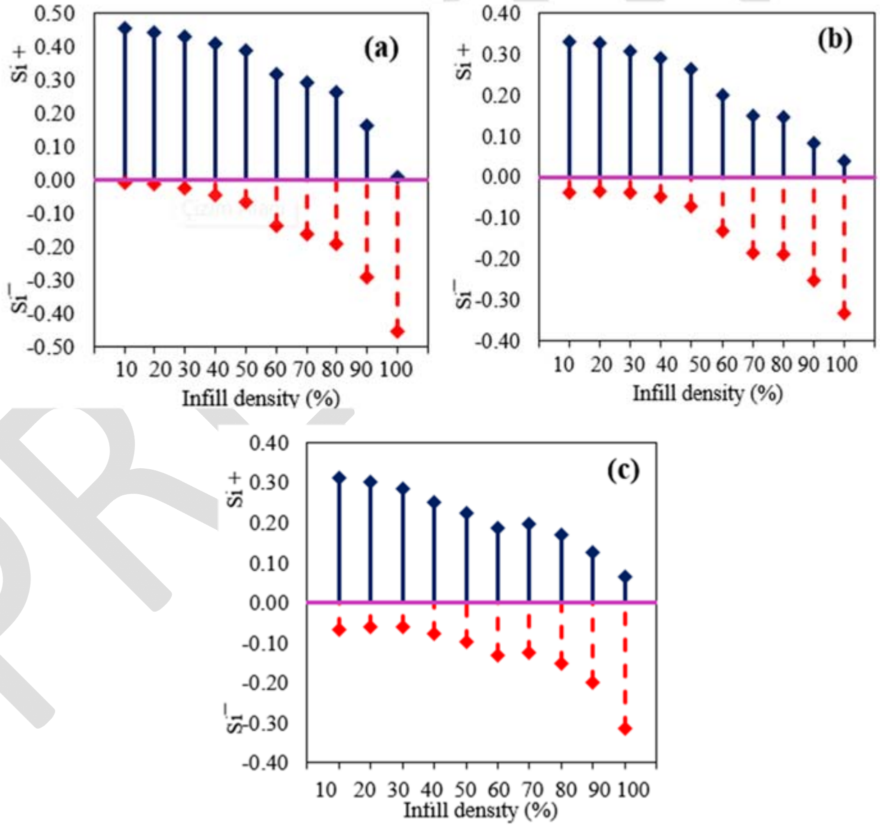


*Figure 8 - The graphical representation of TOPSIS optimization results of aggregates: (a) 8 mm-diameter, (b) 12 mm-diameter, and (c) 16 mm-diameter*

#### *3.1.1. Weighting Sensitivity Analysis Of Infill Density Selection*

**Table 4** reports the sensitivity analysis of several multi-criteria decision approaches used to determine the optimal infill density of the 3DPAs. Across every aggregate diameter and under all objective weighting schemes, the 100% infill-density emerged as the optimal configuration. Both the entropy and CRITIC methods assigned the greatest weight to PCS, reflecting their dominant variability over the infill range, and the TOPSIS and VIKOR rankings showed near-perfect agreement (Spearman rank correlation $\rho$ = 0.99-1.00). This convergence across independent weighting and ranking methods confirms that the identified optimum is robust and method independent.

The dependence of the optimum on the relative importance of the criteria was mapped further through a continuous weight-sensitivity analysis, in which the weight assigned to PCS was varied from 0 to 1 and the remaining weight was divided equally between particle density and cost (**Figure 9**). For each aggregate diameter, the optimal infill density underwent a binary transition between the minimum (10%) and maximum (100%) configurations, and no intermediate infill became optimal under any weighting. This behaviour follows directly from the monotonic increase of all three criteria with infill density, which constrains the optimum to an endpoint. Notably, the weight obtained from both objective methods lies well within the region in which the 100% configuration is optimal (**Figure 9**), which also reinforces the robustness of the selection.

Because PCS, density, and cost all increase linearly with infill, the unconstrained optimization necessarily converges to an extreme configuration. A physically meaningful lightweight optimum therefore requires a minimum strength requirement reflecting the intended civil engineering application. To define this ground, the PCS values reported for artificial lightweight aggregates in the literature were considered. In their comprehensive review, Ren et al. [33] reported that the individual PCS of most artificial aggregates is typically below 10 MPa. For instance, approximately 5 MPa for cold-bonded fly-ash aggregates and around 8 MPa for sintered fly-ash aggregates are reported, whereas high-performance systems (e.g., sintered pellets with bentonite, or alkali-activated fly ash-slag aggregates) can attain 22-23 MPa. Accordingly, a minimum PCS of 10 MPa was adopted as the strength ground for the constrained optimization (**Table 4**), representing the border between aggregates of limited structural value and those suitable for lightweight concrete. Under this constraint, the optimal infill density became markedly lower than the 100% identified by the unconstrained objective methods and was found to be size-dependent: 30%, 60%, and 50% for the 8, 12, and 16 mm aggregates, respectively. This indicates that a substantially lighter and less material-intensive aggregate would suffice to produce structural-grade lightweight concrete when minimal density and cost govern the design intent.

These findings integrate objective optimization with the perspective of lightweight design. The 100% infill density utilized in the present concrete mixtures signifies the high-performance limit of a continuously adjustable property range, while a 30-60% infill provides the optimal balance for applications prioritizing lightweight characteristics. The ability to intentionally choose along this range, balancing mechanical capacity with density and cost, is a primary advantage of additively manufactured 3D-printed aggregates compared to natural and traditional artificial aggregates, whose interior structures are uncontrollable.

*Table 4 - Sensitivity analysis results of infill-density of 3DPAs*

| Approach | Basis | 8 mm | 12 mm | 16 mm |
|---|---|---|---|---|
| TOPSIS – Entropy weights | Objective | 100% | 100% | 100% |
| TOPSIS – CRITIC weights | Objective | 100% | 100% | 100% |
| VIKOR- Entropy weights | Objective | 100% | 100% | 100% |
| Constrained (min, density and cost, PCS ≥ 10 MPa) | Subjective | 30% | 60% | 50% |

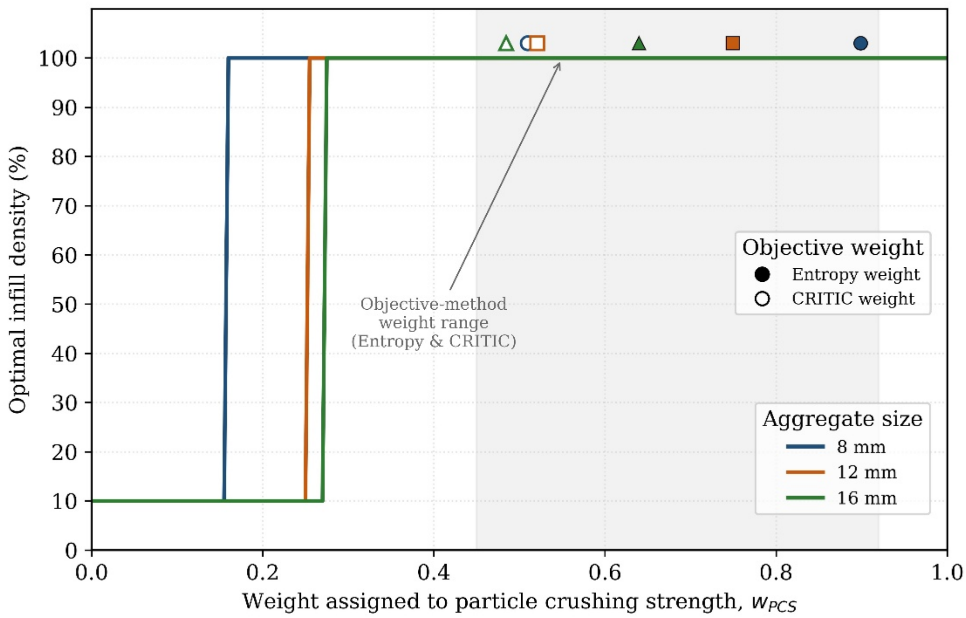


*Figure 9 – The continuous weight-sensitivity analysis: optimal infill density versus the weight assigned to PCS. Symbols at the top indicate the PCS weight values derived from the entropy (filled) and CRITIC (open) weighting methods for each aggregate size (circle = 8 mm, square = 12 mm, triangle = 16 mm)*

### 3.2. Flowability

The influence of NPA and 3DPA on the flow characteristics of fresh LWACs is illustrated in **Figure 10**. The measured flow values ranged from 88% to 115%, demonstrating a clear dependence on both the type and geometry of the coarse aggregate. The "PMC" mixture incorporating NPA exhibited moderately higher flowability compared to those containing 3DPAs. This enhancement is attributed to the pre-soaking of pumice particles prior to mixing. Owing to their highly porous structure, the saturated pumice aggregates gradually released a portion of the absorbed water into the fresh concrete, effectively increasing the available free water content and consequently improving flowability. The flow values measured for mixtures incorporating spherical, edged, and irregular artificial aggregates were 108%, 101%, and 88%, respectively, indicating a clear geometry-dependent trend. The superior flowability observed in mixtures with spherical (SPH) and edged (EDG) aggregates can be attributed to the reduced interparticle friction associated with their perfectly designed and geometrically uniform shapes (see **Figures 4-5**). In contrast, the irregular particle morphology of the IRR aggregates promoted mechanical interlocking and increased interparticle friction, thereby diminishing packing efficiency and lowering mixture fluidity. Cao et al. [34] reported similar findings, noting that the use of angular aggregates, such as manufactured sand and gravel enhances internal friction and interlocking, which ultimately reduces the slump value of concrete.

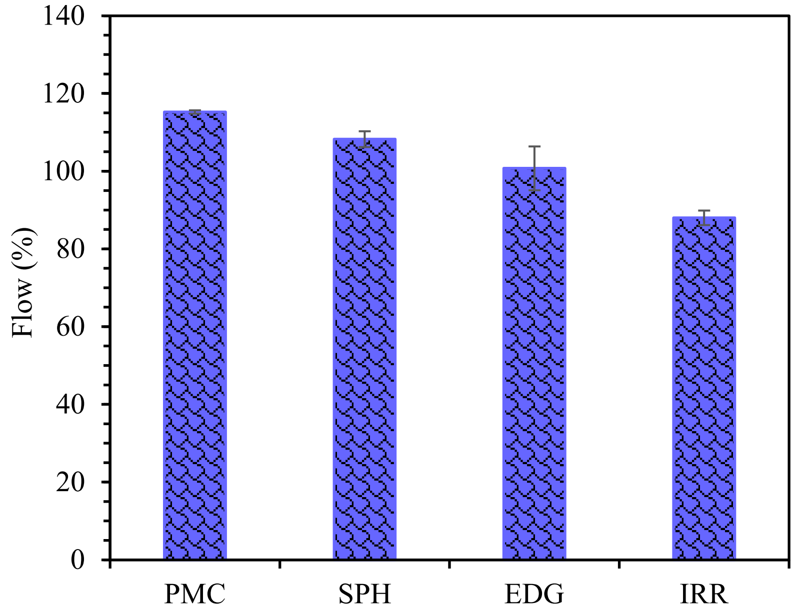


*Figure 10 - The flow results of fresh LWACs*

### 3.3. Compressive Strength and Hardened Density

**Figure 11** depicts the compressive strength development of LWAC specimens. The compressive strength results demonstrate a clear and significant advantage for the concretes incorporating 3DPAs over the NPA reference. At 28 days of curing, the PMC mix achieved a baseline compressive strength of 18.6 MPa. In contrast, the SPH, EDG, and IRR mixtures exhibited notably superior 28-day compressive strengths of 24.9 MPa, 23.2 MPa, and 21.3 MPa, representing respective increases of 34.1%, 25.0%, and 14.7% compared to the reference PMC concrete. A comparable tendency was evident at the early curing stage; after 7 days, the SPH mixture exhibited a 60.4% higher compressive strength than the PMC mixture. The relatively higher compressive strength observed in the concretes containing 3DPAs, regardless of their geometric shape, can be primarily attributed to the inherent physical and mechanical characteristics of the printed particles. NPA is characterized by a highly porous internal structure exhibiting significant intrinsic porosity, which fundamentally limits its individual crushing resistance and creates weak zones within the concrete matrix. Conversely, the 3D-printed polymer aggregates possess substantially higher individual particle strength and lower overall porosity, as illustrated in **Figure 7**. As a result of the optimized printing infill density determined via the TOPSIS method, these artificial aggregates form a stronger, more resilient load-bearing skeleton within the cementitious matrix. This denser internal aggregate structure directly prevents early particle crushing under compressive loads, thereby elevating the strength of the concrete.

Furthermore, the geometry of the 3DPAs notably influenced the mechanical properties of concretes. Among the 3D-printed geometries, the spherical geometry yielded the highest compressive strength. This indicates that the spherical shape likely facilitated a more homogeneous stress distribution and reduced localized stress concentrations at the interfacial transition zone (ITZ) under compressive loading, whereas the sharp angles of the edged and irregular shapes may have induced localized stress micro-cracking despite potentially aiding in mechanical interlocking [35,36]. This is consistent with previous studies reporting that angular coarse aggregates promote stress concentration and earlier crack initiation under load [35,37]. It should be noted, however, that other works report that increased angularity can enhance compressive strength through improved mechanical interlocking [35]. The predominance of the stress-concentration mechanism over the interlocking effect in the present LWAC system is attributed to the smooth, non-reactive surface and controlled geometry of the 3D-printed polymeric aggregates. This represents a divergence from natural aggregate systems in which surface roughness and interlocking govern the mechanical response.

A further distinctive feature of strength development (**Figure 11**) is the contrast in 7-to-28-day strength gain between the mixtures. The pumice control exhibits a substantial later-age increase, whereas the 3DPA mixtures attain the majority of their strength by 7 days with comparatively limited subsequent gain. This behaviour can be attributed to two interrelated mechanisms. First, the pre-soaked pumice acts as an internal water reservoir that gradually releases moisture into the surrounding paste, sustaining cement hydration at later ages and promoting continued densification of the matrix and its ITZ [38]. The impermeable PLA aggregates, by contrast, neither absorb nor release water and therefore provide no internal curing, so the later age hydration and the associated strength gain of the 3DPA mixtures is correspondingly less pronounced. Second, the development of mechanical strength in lightweight concrete depends largely on the ITZ characteristics or the PCS value of the aggregate. While the ITZ in porous pumice aggregate develops over time as the voids in the aggregate fill with hydration products [39], this development is negligible in concrete containing 3DPA due to its non-porous structure. The combination of these effects explains the markedly higher early-age strength and the more modest later-age development observed for the artificial-aggregate concretes.

**Figure 12** illustrates the hardened density results of LWACs. The 28-day hardened density of the concretes ranged from 1798 kg/m$^3$ to 1953 kg/m$^3$. While the reference, PMC mix, exhibited the lowest density of 1798 kg/m$^3$, the incorporation of 3DPAs resulted in a moderate increase in hardened density, yielding values of 1936 kg/m$^3$, 1941 kg/m$^3$, and 1953 kg/m$^3$ for the SPH, EDG, and IRR mixes, respectively. Despite this slight density increase relative to the PMC mix, all concrete mixtures maintained hardened densities below 2000 kg/m$^3$. Consequently, the concretes incorporating 3DPAs can be classified as LWAC as per the TS EN 206 standard [40], confirming the viability of utilizing optimized FDM-printed inclusions for weight-reduction applications in structural engineering.

To comprehensively evaluate the structural efficiency of the developed lightweight concretes, the strength-to-density ratio (specific strength) was analyzed in **Figure 12**. The SPH mix exhibited the highest specific strength value of 12.9 (g/cm$^3$.MPa), followed by EDG (12 g/cm$^3$.MPa), IRR (10.9 g/cm$^3$.MPa), and the reference PMC (10.3 g/cm$^3$.MPa). These specific strength findings confirm that while 3DPAs marginally increase the density of the concrete compared to the highly porous NPA, the substantial gains in compressive strength effectively compensate for the added mass. Ultimately, the integration of spherical 3DPAs provides the most optimal balance between lightweight characteristics and structural capacity.

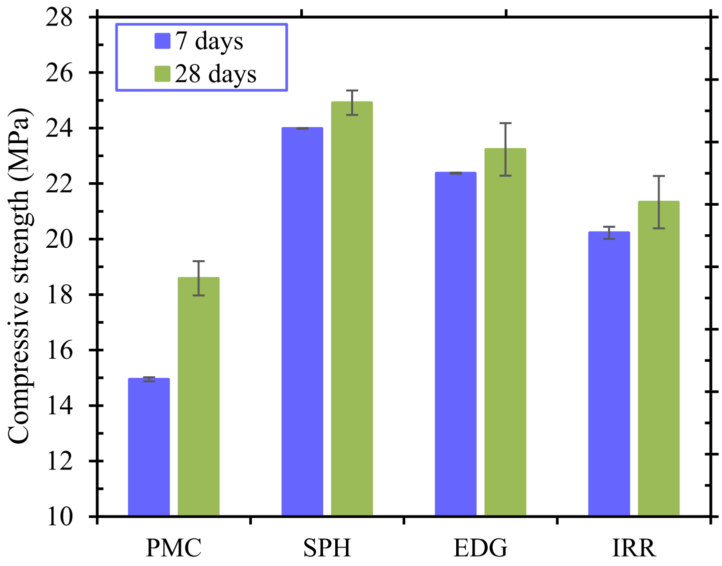


*Figure 11 - Compressive strength development of LWACs*

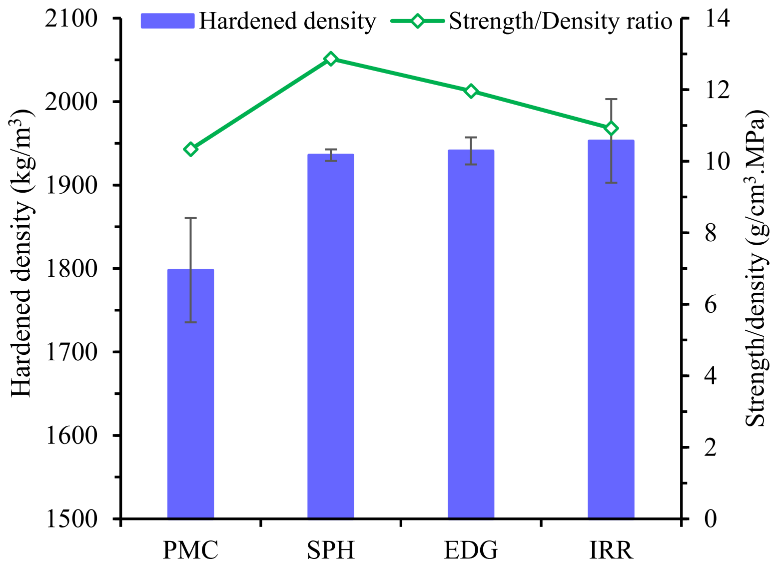


*Figure 12 - Density and specific strength of LWACs*

### 3.4. Physical Properties

#### *3.4.1. Water Absorption and Open Porosity*

The long-term durability and overall performance of LWACs are strongly governed by their open/interconnected pore structure, which dictates the ingress of moisture and chemically aggressive agents. To assess these characteristics, the 28-day water absorption and open porosity values of the LWAC mixtures were measured and the results are presented in **Figure 13**. The control mixture incorporating NPA exhibited the highest water absorption (3.85%) and open porosity (6.92%). This outcome is consistent with the intrinsic nature of pumice, whose highly cellular and interconnected pore structure, stemming from its volcanic origin, substantially enhances the capillary pore network within the hardened concrete. In contrast, the mixtures produced with 3DPAs demonstrated markedly lower water absorption and porosity values. The SPH, EDG, and IRR mixes exhibited water absorption of 2.63%, 2.68%, and 2.93%, corresponding to reductions of approximately 31.7%, 30.4%, and 23.9%, respectively, when compared with the PMC mix. A consistent and similar pattern was also observed in the open porosity measurements, where the SPH (5.08%), EDG (5.25%), and IRR (5.70%) concretes demonstrated significant decreases of 26.6%, 24.1%, and 17.6%, respectively, compared to the PMC mix. The ameliorated absorption characteristics of the LWAC containing 3DPAs can be primarily attributed to the polymeric nature of the FDM material that is inherently impermeable compared to the highly absorptive pumice. The hydrophobic shell of 3DPAs effectively restricts continuous capillary water transport through the aggregate phase. Consequently, water penetration in these mixtures is predominantly confined to the cement paste matrix and the ITZ, rather than permeating the aggregates themselves. Furthermore, the geometric morphology of the artificial aggregates played a negligible role in the water absorption of LWACs. These findings are consistent with previous reports that the polymeric phase in plastic-aggregate systems is hydrophobic and exhibits negligible water absorption [41], and that the application of an impermeable plastic coating to porous aggregates substantially lowers their water absorption [42].

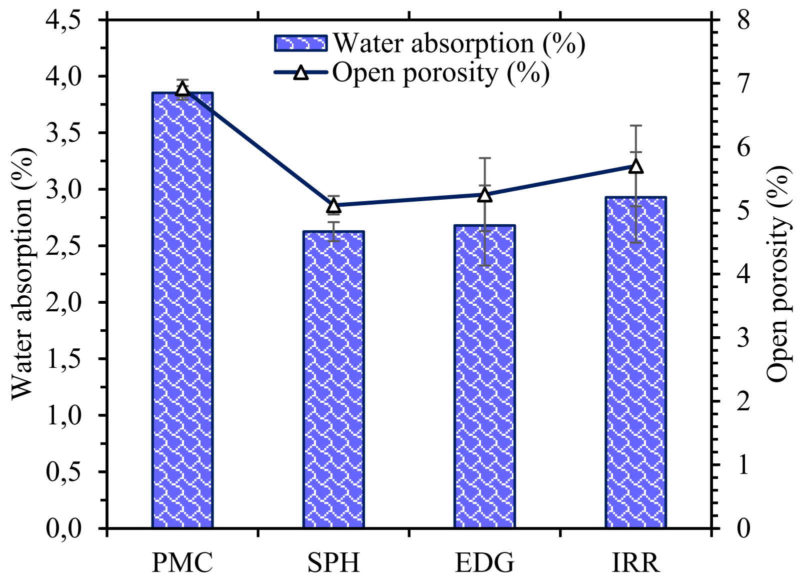


*Figure 13 - Water absorption and open porosity of LWAC mixtures*

### *3.4.2. Capillary Sorptivity*

The capillary water sorptivity results of LWAC mixtures are illustrated in **Table 5**. The capillary absorption is typically assessed in two distinct phases as initial sorptivity, governed by the rapid filling of capillary pores, and secondary sorptivity, which reflects the slower, long-term permeation of water into large air voids and microcracks [43,44]. The initial sorptivity coefficients of the LWAC mixtures were measured within the range of $15 \times 10^{-4}$ to $22 \times 10^{-4}$ mm/s$^{0.5}$, whereas the secondary sorptivity values varied between $4.0 \times 10^{-4}$ and $7.5 \times 10^{-4}$ mm/s$^{0.5}$. Among all mixtures, the PMC mix exhibited the highest initial sorptivity, while also presenting the lowest secondary sorptivity value among the tested mixes. When the concrete surface is exposed to water, the inherent cellular network of the pumice acts as a direct conduit, accelerating the capillary suction rate during the initial hours of exposure, as illustrated in **Figure 14**. On the other hand, since the pores of pumice particles rapidly saturate during the initial phase, the subsequent long-term absorption capacity, accordingly secondary sorptivity is significantly diminished.

The initial sorptivity values of EDG, SPH, and IRR mixes were found approximately 31.8%, 15.9%, and 6.8% lower than the PMC mix, respectively. This decline highlights the protective barrier effect provided by the impermeable polymeric outer shell of the 3DPAs.

Since water cannot readily permeate the aggregate particles themselves, capillary transport is strictly confined to the matrix and the ITZ. On the other hand, the effect of 3DPA geometry on the sorptivity results indicates that the presence of elongated irregular 3DPA particles (in the IRR mix) creates more heterogenous ITZ and microcracks between the aggregate particles and the matrix, which increases the initial sorptivity compared to others, as shown in **Figure 14**.

*Table 5 - Water sorptivity results of LWAC mixes*

| Concrete ID | Initial sorptivity ($mm/s^{0.5}$) ($\times10^{-4}$) | Secondary sorptivity ($mm/s^{0.5}$) ($\times10^{-4}$) |
|---|---|---|
| PMC | 22 | 4 |
| SPH | 18.5 | 7.5 |
| EDG | 15 | 7 |
| IRR | 20.5 | 6.5 |

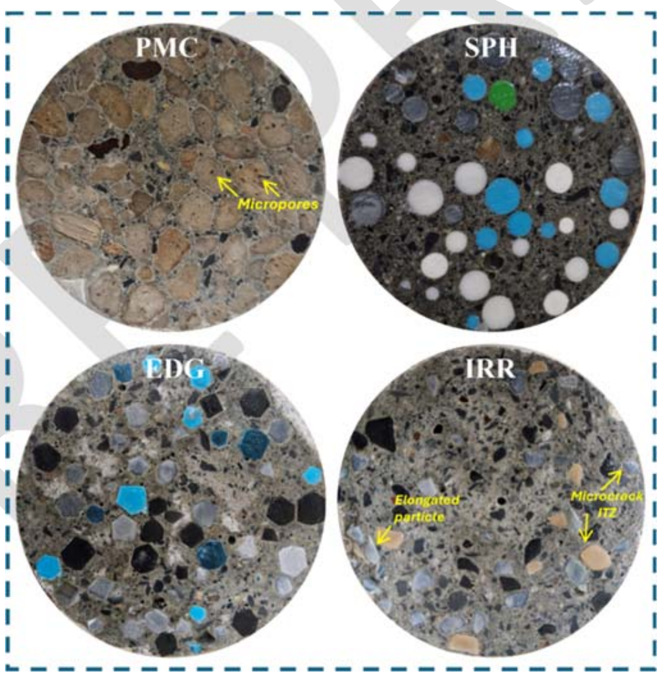


*Figure 14 - The cross-sectional appearances of LWACs*

#### *3.4.3. Abrasion Resistance*

The evolution of height and mass losses in the LWAC specimens following the abrasion test is presented in **Figure 15**. After completing 16 abrasion cycles, the specimens exhibited height reductions between 0.90% and 1.44% and mass losses ranging from 1.81% to 2.46%. The results clearly indicate that incorporating 3DPAs, regardless of their geometries, enhance the abrasion resistance of LWAC compared to the pumice-based control concrete, as evidenced by a lower height and mass reductions. Accordingly, the total volume loss of PMC, SPH, EDG, and IRR mixes were found to be 8339, 6567, 6386, and 7583 ($mm^3/50\ cm^2$), respectively. These values correspond to remarkable reduction of approximately 23.4%, 21.3%, and 9.1% compared to the PMC reference. Similarly, the PMC concrete exhibited a height loss that was 1.55, 1.30, and 1.60 times more than that of the SPH, EDG, and IRR, respectively. The superior abrasion resistance observed in concretes incorporating 3DPAs primarily arises from their enhanced toughness, elevated particle strength, absence of internal porosity, and non-friable structural characteristics. These aggregates exhibit a greater capacity for elastic deformation and energy absorption, enabling them to endure abrasive and grinding actions without undergoing early fracture. This is consistent with the well-established correlation between aggregate strength/hardness, concrete compressive strength, and abrasion resistance, whereby stronger, denser aggregates and higher-strength matrices exhibit lower abrasive wear [45]. The geometry of the artificial aggregates was also found to significantly influence the abrasion resistance of the LWAC mixtures. The highest resistance to abrasion was achieved in concretes incorporating spherical and edged aggregates. This improved performance is likely attributable to the reduced contact area formed between these well-defined particle shapes and the abrasion surface, which minimizes abrasive interaction during testing. This effect, combined with the uniformity of their geometry, may account for the superior abrasion resistance observed in these mixtures. These findings are consistent with previous studies indicating that aggregates possessing harder or more stable surface characteristics can substantially enhance the abrasion resistance of concrete [46,47]. It is noteworthy that the volumetric loss values of around 6500 ($mm^3/50\ cm^2$) achieved by the EDG and SPH concretes are exceptionally competitive for lightweight and normal weight concretes, presented in the literature [45,48–50].

**Figure 16** presents the surfaces of the LWAC specimens following the abrasion test. The 3D-printed aggregates exposed at the abraded surface retained their printed morphology, with the characteristic FDM layer lines remaining clearly discernible and no indication of melting, softening, rounding by flow, or thermal deformation. This confirms that the chosen drying protocol and following abrasion did not compromise the integrity of the polymer phase. Furthermore, it is worth noting that localized surface scaling was observed in some certain specimens, predominantly in regions adjacent to the larger coarse 3DPA particles.

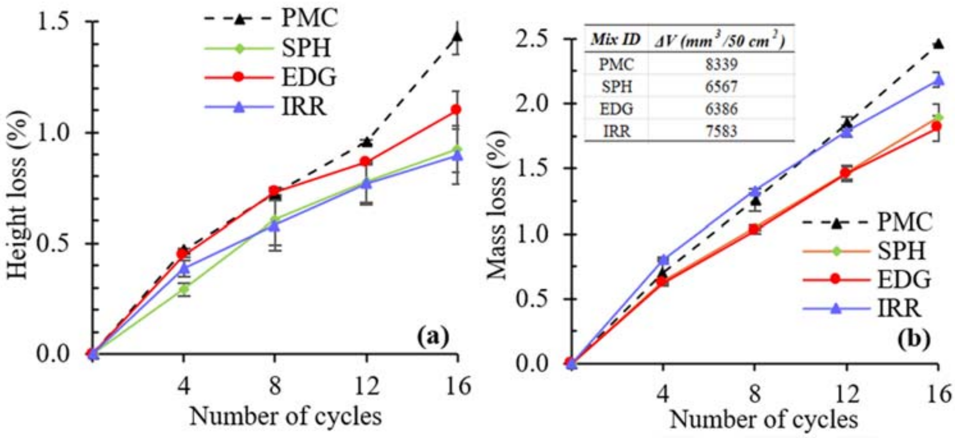


*Figure 15 - The abrasion test results of LWAC mixes: (a) height loss and (b) mass loss*

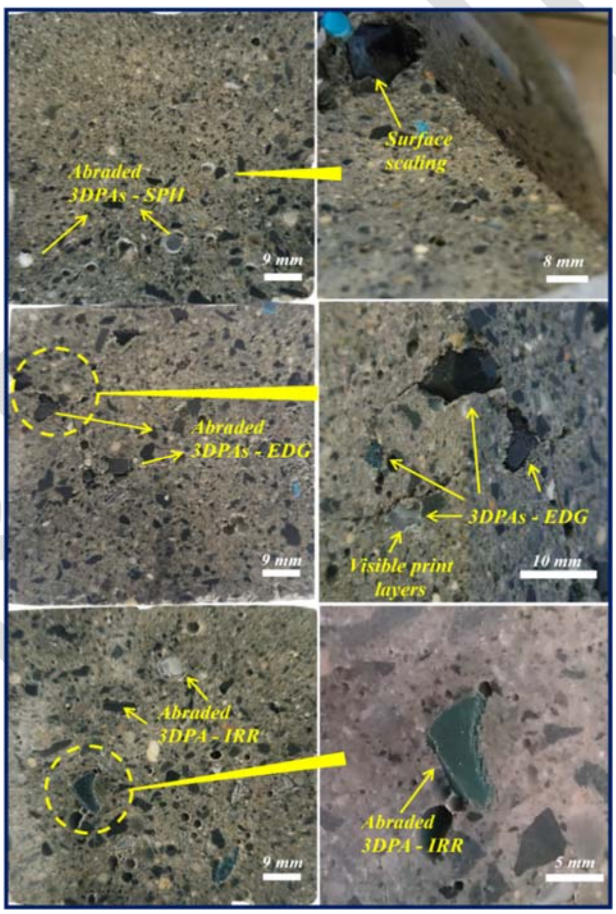


*Figure 16 - The appearance of abraded LWAC specimen containing 3DPA*

### 3.5. Chloride Migration Resistance

**Figure 17** depicts the impact of lightweight coarse aggregate type on the chloride migration resistance of LWAC mixes. The experimental results reveal a profound disparity in chloride permeability between the pumice containing LWAC and the mixtures containing artificial aggregates. The PMC exhibited an exceptionally high chloride migration coefficient of $25.5\times10^{-12}$ ($m^2/s$). This poor resistance is directly correlated with the previously discussed water absorption and open porosity findings. The highly cellular, interconnected pore structure of the NPAs acts as a direct waterway, providing minimal physical resistance to the transport of chloride ions through the concrete matrix under an electrical field. On the other hand, the utilization of 3DPAs resulted in a powerful enhancement in chloride migration resistance of LWAC mixes. The $D_{nssm}$ for the SPH, EDG, and IRR mixtures sharply decreased to $3.7\times10^{-12}$, $4.6\times10^{-12}$, and $7.7\times10^{-12}$ ($m^2/s$), respectively. These values represent remarkable reductions of approximately 85.6%, 82.1%, and 70.0% relative to the PMC reference mix. This important decrease in chloride penetrability is mainly driven by the physical barrier effect induced by the 3DPAs. Unlike the highly permeable pumice, the polymeric nature of particles is inherently non-porous and completely impermeable to ionic transport. Consequently, the 3DPAs act as solid, impenetrable barriers within the matrix. The chloride ions are thus forced to navigate exclusively through the cement paste and the ITZ, significantly increasing the tortuosity of the transport path and effectively hindering chloride migration. This is well in line with numerical and experimental studies demonstrating that impermeable aggregates reduce ionic transport through dilution and tortuosity effects, and that aggregate shape modulates the transport path [51,52]. Moreover, the geometric configuration of the artificial aggregates exerted a measurable influence on the chloride migration characteristics of the LWAC mixtures. Among the tested concretes, the SPH mixture exhibited the greatest resistance to chloride penetration, while the IRR mixture showed comparatively lower resistance. As illustrated in **Figure 14**, the smooth and well-rounded morphology of the spherical aggregates in SPH, and to a similar extent in EDG, promotes a more uniform distribution of cement paste and the formation of a denser, higher-quality ITZ with fewer defects. In contrast, the irregular geometry of the IRR aggregates somehow decreases the matrix continuity and reduces the effectiveness of this physical barrier, thereby allowing more favorable pathways for chloride ingress.

The classification of chloride penetration according to the $D_{nssm}$ coefficient proposed by [53] is also given in **Figure 17.** According to this classification, SPH and EDG concretes exhibited superior resistance against chloride permeability, with “very low” $D_{nssm}$ values ($< 5\times10^{-12}$ ($m^2/s$)), while IRR concrete also showed good resistance against chloride migration with “low” $D_{nssm}$ value ($5\text{-}10\times10^{-12}$ ($m^2/s$)). In contrast, the reference LWAC with NPA presented a remarkably low chloride migration resistance with a “high” $D_{nssm}$ value of higher than $15\times10^{-12}$ ($m^2/s$).

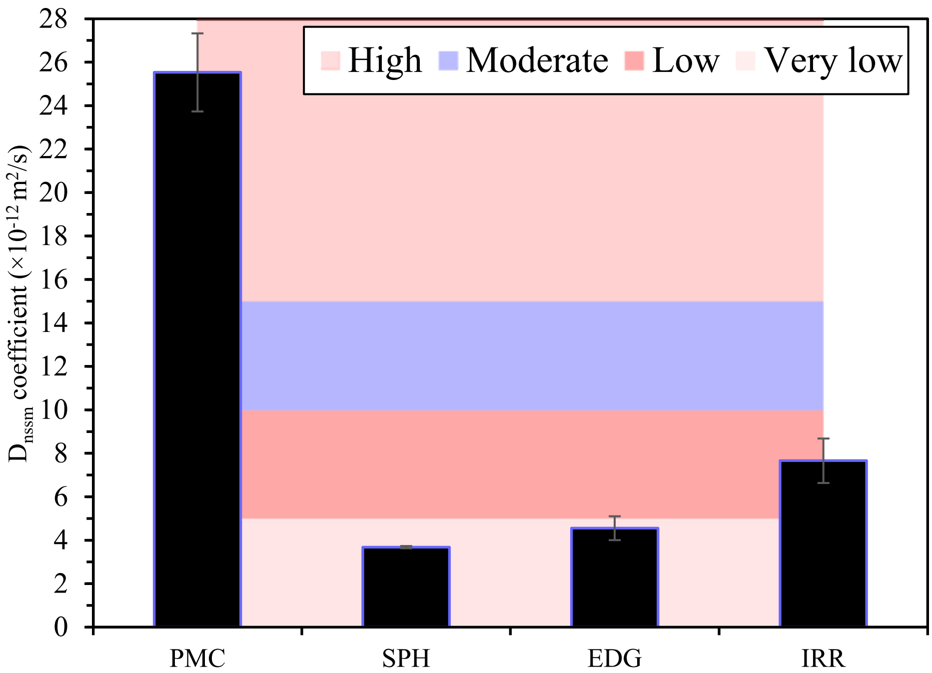


*Figure 17 - The chloride migration resistance of LWAC specimens*

### 3.6. Economic and Production Feasibility Considerations

To assess the practical applicability of the proposed 3DPA production, the laboratory-scale unit costs were scaled up to a representative 1 $m^3$ concrete volume. In the investigated mixtures, each $m^3$ of LWAC consumes approximately 313 kg of PLA material. Taking a representative virgin-PLA filament price of US$15/kg, the feedstock alone accounts for US$4,695/$m^3$. The printing energy, derived from the measured laboratory printing rate and an electricity tariff of US$0.00025/min, adds a further US$155/$m^3$, roughly 3% of the total, so that the aggregate production cost reaches approximately US$4,850/$m^3$. For comparison, natural pumice carries a processed unit value of the order of about US$44/t [54], corresponding to roughly US$15 per $m^3$ of concrete at the present mix proportions. Moreover, the operational production cost of sintered fly-ash aggregate has been reported at approximately 30-55 US$/t [55]. On both a per-mass and per-concrete-volume basis, the virgin-PLA 3DPA is therefore one-to-two orders of magnitude more costly than conventional lightweight aggregates (**Table 6**). On the other hand, the utilization of recycled plastics (recycled PET: ~1.5 US$/kg, recycled PLA: 4-6 US$/kg) in 3D-printing process significantly reduced the overall cost of LWAC production compared to commercially available virgin PLA counterparts. In addition, incorporating various recyclable polymer sources apart from PET or PLA into the 3D-printing feedstock may bring its cost toward parity with conventional alternatives in the future.

A precise time estimation of large-scale 3DPA production is hard to estimate, as the printing throughput is governed by a multiplicity of interacting parameters, such as infill density and pattern, machine kinematics, acceleration and jerk limits, nozzle diameter, and the number of print heads. Since these parameters cannot be reliably extrapolated from single-machine laboratory-scale data, a hypothetical assessment of production time is carried out to illustrate both the current limitations and the prospective scalability of the presented 3DPA production approach. **Table 7** presents the estimated printing time required to produce the 3DPA for 1 $m^3$ of concrete. The required printing time was estimated for three classes of equipment spanning the range of available deposition rates, including the desktop type single-nozzle FDM system used in this study, industrial pellet-based fused-granulate fabrication (FGF) printers, and large-format Big-Area Additive Manufacturing (BAAM) systems. For each class, lower and upper throughput bounds were considered, and the values are derived from existing literature and current manufacturer reports [56,57]. With a desktop type single-nozzle system device, fabricating the 313 kg of 3DPA required for 1 $m^3$ of concrete at 100% infill would require approximately 1,040 h at the maximum demonstrated single-nozzle deposition rate and 10,400 h at the conventional size cheap devices. As expected, this also confirms that single-nozzle FDM systems, regardless of optimization, are fundamentally required multiple machines with continuous printing for production-scale aggregate manufacturing. In contrast, industrial pellet-based systems, which are documented to raise deposition rates by more than two orders of magnitude relative to conventional filament extrusion, reduce this time dramatically [58,59]. The corresponding printing times to produce 1 $m^3$ 3DPA-concrete are calculated around 12.5-104 h for FGF printers and as little as 6-70 h for BAAM systems. These figures are necessarily indicative and represent optimistic upper bounds, since the rated capacities assume continuous deposition rather than the fabrication of numerous discrete particles. Importantly, the highest throughputs are attained only with large nozzle or bead diameters (frequently ≥1 mm, up to several millimetres), which inherently limit the minimum aggregate diameter size and geometric fidelity that can be reproduced. Faithfully reproducing the morphology of the relatively small 4-8 mm aggregates would necessitate smaller nozzles, so the throughput realistically achievable for aggregate production would lie below the stated upper limits. Notwithstanding this constraint, the analysis demonstrates that the throughput barrier is governed by equipment scale and nozzle resolution rather than by the additive-manufacturing principle itself, and that industrial-scale or recycled-feedstock systems could render the approach substantially more viable [60].

Overall, the objective of this study is not to propose 3DPA as a cost-parity replacement for bulk lightweight aggregates. Rather, it serves as a proof-of-concept demonstrating that additive manufacturing offers unique control over particle geometry, internal porosity, and crushing strength, allowing quantify the resulting improvements in mechanical performance and durability. The economic and output feasibility of large scale 3DPA production will be contingent on two intersecting advancements. One is substituting virgin PLA with recycled or waste-derived thermoplastics, such as post-consumer PLA or recycled-PET, which can diminish feedstock costs by approximately an order of magnitude and enhance the environmental profile. Another is the ongoing transition towards high-efficiency additive manufacturing platforms. Under these conditions, and for high-value applications where durability or geometry is critical, the additive-manufacturing route becomes increasingly justifiable for specialised rather than commodity use.

*Table 6 – Cost-comparison of various lightweight aggregate sources*

| LWA type | Production route | Cost ($/m$^3$ concrete) | Process maturity |
|---|---|---|---|
| Pumice (NPA, reference) | Quarried, pre-soaked | ~15-20 | High |
| Sintered fly ash | Pelletizing + sintering | ~10-40 | Modarate |
| 3DPA (Commercial PLA, FDM) | Filament FDM + Electricity (This study) | ~4850 | Emerging, currently low |
| 3DPA (Recycled feedstock) | Recycled PET, Recycled PLA | ~375-1250 | Developing, rapidly improving |

*Table 7 – Printing time estimation for 3DPA (Single Device, 1 m$^3$ LWAC, 100% infill, 313 kg PLA)*

| Printing system | Printing capacity (low-high) | Time per m$^3$ of LWAC |
|---|---|---|
| Desktop type single-nozzle FDM (This study) | 0.03-0.3 kg/h | ~1040 - 10400 h |
| Industry pellet FGF printer | 3-25 kg/h | ~12.5 - 104 h |
| Large-format BAAM | 4.5-50 kg/h | ~6 - 70 h |

## 4. CONCLUSIONS

This paper explored a new category of lightweight artificial aggregates manufactured using FDM-based 3D-printing and systematically assessed their impact on the fresh, mechanical, physical, and durability properties of LWAC. By integrating multi-criteria optimization via TOPSIS approach, the properties of 3D-printed artificial aggregates were initially optimized, and the resulting concrete properties are investigated in detail. Based on the experimental findings following key conclusions can be drawn:

- The feasibility of producing artificial aggregates with low density (about 0.5-1 g/cm$^3$) and high mechanical strength (PCS value of up to 42 MPa) in various shapes and morphologies using 3D-printing technology has been successfully demonstrated. The TOPSIS and VIKOR-based optimization approach identified 100% infill density as the most suitable printing configuration for all aggregate size ranges. This configuration maximized particle crushing strength while maintaining acceptable density and production cost, highlighting the value of decision-making algorithms in tailoring additive-manufactured aggregates for LWAC applications.
- 3D-printed aggregates significantly ameliorated compressive strength of LWACs relative to natural pumice-containing concrete. After 28 days, concretes incorporating spherical, edged, and irregular aggregates achieved strength gains of

34%, 25%, and 15%, respectively, compared with the pumice reference, which can be directly linked to the higher PCS and low porous structure of the artificial aggregates. In addition, all concrete mixtures containing 3D-printed aggregates satisfied the lightweight concrete requirement (<2000 kg/m$^3$). LWAC mixtures containing spherical and edged artificial aggregate particles exhibited the highest specific strength values.

- Water absorption, open porosity, and capillary sorptivity were substantially reduced in concretes incorporating 3D-printed aggregates compared to natural pumice-based concrete. The impermeable polymeric shell of the 3D-printed artificial aggregates lowered water absorption by up to 32% and open porosity by 27% compared to pumice-based LWAC. Initial sorptivity also decreased markedly for the SPH and EDG mixtures due to the absence of permeable pores in aggregates. The IRR mixture, however, exhibited slightly higher initial sorptivity than the other artificial-aggregate concretes, attributable to geometry-induced microcrack formations and local discontinuities around elongated aggregate edges.
- Abrasion resistance improved significantly for all 3D-printed aggregate LWAC mixtures, with volumetric loss reductions reaching 23% relative to the pumice mixture. The enhanced particle toughness and the absence of weak and porous internal structure contributed to superior abrasive wear resistance of LWACs with artificial aggregates. In addition, the impermeable 3D-printed polymeric aggregate phase significantly elongated ion transport pathways and the most pronounced improvement was observed in chloride migration resistance of LWACs. The concretes containing spherical and edged shaped artificial aggregates achieved "very low" chloride migration coefficients ($D_{nssm}$ < 5×10$^{-12}$ m²/s), representing reductions of more than 80% relative to the pumice-based LWAC.
- The conceptual economic and feasibility analysis of 3DPA incorporating LWACs reveals that virgin-PLA 3DPA presently surpasses the expense of traditional lightweight aggregates, with single-nozzle printing throughput serving as the primary obstacle to scalability. Its immediate relevance is thus limited to niche applications where durability or geometry is crucial, dependent on the utilization of recycled polymer feedstocks and the ongoing advancement of advanced additive manufacturing methods. It should also be emphasized that PLA serves here as a representative model feedstock for establishing the additive-manufacturing concept. Its thermal sensitivity restricts the material to ambient, non-fire-critical services, such as non-structural and architectural precast panels, interior partition and cladding elements, and lightweight acoustic barriers. The use of thermally stable engineering thermoplastics or recycled high-temperature thermoplastics represents a direct route to extending the thermal tolerance and broadening the application range of additively manufactured aggregates.

Overall, 3D-printed artificial aggregates represent a transformative alternative to traditional lightweight aggregates like pumice, offering tunable geometry, controlled density, and superior particle strength. The precise morphological control enabled by additive manufacturing allows for aggregate design beyond the limitations of natural and conventional artificial aggregates, enabling the controllable LWAC production suitable for durability critical applications. Looking forward, the integration of 3D-printed aggregates into practical construction demands further research on large-scale production feasibility, cost optimization, surface modification strategies to improve the ITZ properties, the use of hybrid or recycled polymers as sustainable feedstocks, and long-term durability performance under freeze-thaw, carbonation, and aggressive chemical environments. In addition, the performances of natural porous lightweight aggregates and 3DPAs should also be compared under same consistency level design approaches instead of constant w/c ratio. These future developments have the potential to establish 3D-printed aggregates as a viable, next-generation materials for use in high-performance LWAC.

**Acknowledgement**

The experimental study was carried out at the Construction Materials Laboratory of Yildiz Technical University.

## References

[1] N. Singh, J. Raza, F. Colangelo, I. Farina, Advancements in lightweight artificial aggregates: typologies, compositions, applications, and prospects for the future, Sustainability 16 (2024) 9329.

[2] G.B. Bekkeri, K.K. Shetty, G. Nayak, Synthesis of artificial aggregates and their impact on performance of concrete: a review, J. Mater. Cycles Waste Manag. 25 (2023) 1988–2011.

[3] Z. Duan, W. Yang, S. Zou, H. Liu, W. Zhao, W. Chen, A critical review on cold-bonded artificial aggregate developed from solid wastes: From granulation analysis to performance evaluation, Journal of Building Engineering 99 (2025) 111588.

[4] S. Islam, G. Ara, U.S. Akhtar, M.G. Mostafa, I. Haque, Z.M. Shuva, A. Samad, Development of lightweight structural concrete with artificial aggregate manufactured from local clay and solid waste materials, Heliyon 10 (2024).

[5] B. Vakhshouri, S. Nejadi, Review on the mixture design and mechanical properties of the lightweight concrete containing expanded polystyrene beads, Australian Journal of Structural Engineering 19 (2018) 1–23.

[6] X. Shang, J. Chang, J. Yang, X. Ke, Z. Duan, Life cycle sustainable assessment of natural vs artificial lightweight aggregates, J. Clean. Prod. 367 (2022) 133064.

[7] A.T. Abdulrasool, S.S. Mohammed, N.R. Kadhim, W.A. Mohammad Hussain, Sustainable materials used as lightweight aggregate:(an overview), in: IOP Conf. Ser. Earth Environ. Sci., IOP Publishing, 2022: p. 012027.

[8] N.A. Conzelmann, M.N. Partl, F.J. Clemens, C.R. Müller, L.D. Poulikakos, Effect of artificial aggregate shapes on the porosity, tortuosity and permeability of their packings, Powder Technol. 397 (2022) 117019.

[9] M. Zhao, M. Zhao, M. Chen, J. Li, D. Law, An experimental study on strength and toughness of steel fiber reinforced expanded-shale lightweight concrete, Constr. Build. Mater. 183 (2018) 493–501.

[10] Y.O. Özkılıç, A.N. Beskopylny, S.A. Stel'makh, E.M. Shcherban, L.R. Mailyan, B. Meskhi, A. Chernil'nik, O. Ananova, C. Aksoylu, E. Madenci, Lightweight expanded-clay fiber concrete with improved characteristics reinforced with short natural fibers, Case Studies in Construction Materials 19 (2023) e02367.

[11] A. Terzić, L. Pezo, V. Mitić, Z. Radojević, Artificial fly ash based aggregates properties influence on lightweight concrete performances, Ceram. Int. 41 (2015) 2714–2726.

[12] Y. Liang, B. Guan, T. Cao, G. Liu, P. Tang, M. He, M.F. Cheira, A.M. Rashad, Study on the properties of an excess-sulphate phosphogypsum slag cement stabilized base-course mixture containing phosphogypsum-based artificial aggregate, Constr. Build. Mater. 409 (2023) 134095.

[13] N. Kabay, A.B. Kızılkanat, B. Akturk, Y. Kahraman, Lightweight cement-based composites incorporating hollow glass microspheres: Fresh and hardened state properties, Teknik Dergi 33 (2022) 11543–11567.

[14] J. Liu, C. Shi, N. Farzadnia, X. Ma, Effects of pretreated fine lightweight aggregate on shrinkage and pore structure of ultra-high strength concrete, Constr. Build. Mater. 204 (2019) 276–287.

[15] .K. Yew, M.C. Yew, J.H. Beh, F.W. Lee, S.K. Lim, Y.L. Lee, J.H. Lim, K.I.S.A. Kabeer, Effect of pre-soaking treatment method of plant-based aggregate on the properties of lightweight concrete—preliminary study, Coatings 13 (2023) 864.

[16] W. Li, D. Wang, B. Chen, K. Hua, Z. Huang, C. Xiong, H. Yu, Preparation of artificial pavement coarse aggregate using 3D printing technology, Materials 15 (2022) 1575.

[17] Z. Chen, J. Li, C. Luo, H. Cui, W. Li, Research and application of high-performance artificial aggregates based on 3D printing, Front. Mater. 13 (2026) 1797017.

[18] Y. Chen, Y. Zhang, B. Pang, Z. Liu, G. Liu, Extrusion-based 3D printing concrete with coarse aggregate: Printability and direction-dependent mechanical performance, Constr. Build. Mater. 296 (2021) 123624.

[19] M. Hematibahar, A. Hasanzadeh, M. Kharun, A.N. Beskopylny, S.A. Stel'makh, E.M. Shcherban', The Influence of Three-Dimensionally Printed Polymer Materials as Trusses and Shell Structures on the Mechanical Properties and Load-Bearing Capacity of Reinforced Concrete, Materials 17 (2024). https://doi.org/10.3390/ma17143413.

[20] Turkish Standards Institution, Tests for mechanical and physical properties of aggregates - Part 6: Determination of particle density and water absorption, Ankara, 2022.

[21] M. Rizwee, D. Kumar, Contribution of geometrical infill pattern on mechanical behaviour of 3D manufactured polylactic acid specimen: experimental and numerical analysis, Progress in Rubber, Plastics and Recycling Technology 41 (2025) 331–351.

[22] B. Pernet, J.K. Nagel, H. Zhang, Compressive strength assessment of 3D printing infill patterns, Procedia CIRP 105 (2022) 682–687.

[23] H. Özkan, N. Kabay, N. Miyan, Properties of cold-bonded and sintered aggregate using washing aggregate sludge and their incorporation in concrete: A promising material, Sustainability 14 (2022) 4205.

[24] D. Diakoulaki, G. Mavrotas, L. Papayannakis, Determining objective weights in multiple criteria problems: The critic method, Comput. Oper. Res. 22 (1995) 763–770.

[25] H. Taherdoost, M. Madanchian, VIKOR method—an effective compromising ranking technique for decision making, Taherdoost, H., Madanchian, M (2023) 27–33.

[26] ASTM International, Standard Test Method for Flow of Hydraulic Cement Mortar, West Conshohocken, PA, 2020.

[27] European Committee for Standardization, Testing hardened concrete - Part 1: Shape, dimensions and other requirements for specimens and moulds, Brussels, 2021.

[28] N. Miyan, T. Omur, N. Kabay, B. Birol, The potential usage of waste ferrochrome slag in alkali-activated mixes, Journal of Building Engineering 75 (2023) 107026. https://doi.org/10.1016/j.jobe.2023.107026.

[29] S. Farah, D.G. Anderson, R. Langer, Physical and mechanical properties of PLA, and their functions in widespread applications — A comprehensive review, Adv. Drug Deliv. Rev. 107 (2016) 367–392. https://doi.org/10.1016/j.addr.2016.06.012.

[30] ASTM International, Standard Test Method for Measurement of Rate of Absorption of Water by Hydraulic-Cement Concretes, West Conshohocken, PA, 2020.

[31] European Committee for Standardization, Concrete paving blocks - Requirements and test methods, Brussels, 2003.

[32] Nordtest, Concrete, mortar and cement-based repair materials: Chloride migration coefficient from non-steady-state migration experiments, Espoo, 1999.

[33] P. Ren, T.-C. Ling, K.H. Mo, Recent advances in artificial aggregate production, J. Clean. Prod. 291 (2021) 125215.

[34] G. Cao, Y. Liu, S. Long, D. Deng, S. Jiang, H. Su, T. Tan, Influence of aggregate shape on the flow properties of fresh concrete, Powder Technol. 415 (2023) 118186. https://doi.org/10.1016/j.powtec.2022.118186.

[35] S.J. Lee, C.H. Lee, M. Shin, S. Bhattacharya, Y.F. Su, Influence of coarse aggregate angularity on the mechanical performance of cement-based materials, Constr. Build. Mater. 204 (2019) 184–192.

[36] Q. Liu, A. Cheng, C. Sun, K. Chen, Y. Wang, W. Li, Effects of aggregate's type and orientation on stress concentration and crack propagation of modeled concrete applied a shear force, Journal of Building Engineering 95 (2024) 110340.

[37] P. Deng, K. Xu, S. Guo, Effects of coarse aggregate morphology on concrete mechanical properties, Journal of Building Engineering 63 (2023) 105408.

[38] J. Castro, L. Keiser, M. Golias, J. Weiss, Absorption and desorption properties of fine lightweight aggregate for application to internally cured concrete mixtures, Cem. Concr. Compos. 33 (2011) 1001–1008.

[39] J. Zhou, Y. Dong, T. Qiu, J. Lv, P. Guo, X. Liu, The microstructure and modification of the interfacial transition zone in lightweight aggregate concrete: a review, Buildings 15 (2025) 2784.

[40] Turkish Standards Institution, Concrete - Specification, performance, production and conformity, Ankara, 2021.

[41] L. Gu, T. Ozbakkaloglu, Use of recycled plastics in concrete: A critical review, Waste Management 51 (2016) 19–42.

[42] W. Ye, S. Li, T. Qiu, X. Cong, Y. Tan, Effects of plastic coating on the physical and mechanical properties of the artificial aggregate made by fly ash, J. Clean. Prod. 360 (2022) 132187.

[43] C.S. Thunuguntla, T.D.G. Rao, Effect of mix design parameters on mechanical and durability properties of alkali activated slag concrete, Constr. Build. Mater. 193 (2018) 173–188.

[44] S. Papatzani, K. Paıne, Nanomontmorillonite Reinforced Fibre Cements and Nanomontmorillonite-Nanosilica Reinforced Mortars, Turkish Journal of Civil Engineering 34 (2023) 43–60.

[45] A. Kılıç, C.D. Atiş, A. Teymen, O. Karahan, F. Özcan, C. Bilim, M. Özdemir, The influence of aggregate type on the strength and abrasion resistance of high strength concrete, Cem. Concr. Compos. 30 (2008) 290–296.

[46] İ.A. Al-akhaly, Engineering properties of basalt coarse aggregates in Hamdan Area, NW Sana'a, Yemen, Jeoloji Mühendisliği Dergisi 42 (2018) 159–174.

[47] T. Omur, A.K. Akpunar, A.B. Bingöl, B. Oktay, C.B. Üstündağ, N. Kabay, The influence of phase change material filled three-dimensional printed artificial aggregates on the properties of blast furnace slag based alkali-activated concrete, Frontiers of Structural and Civil Engineering 19 (2025) 445–457.

[48] N. Kabay, Abrasion resistance and fracture energy of concretes with basalt fiber, Constr. Build. Mater. 50 (2014) 95–101.

[49] E.T. Tunc, A Preliminary Experimental Study on the Comparison of Concrete Strength Tests and Bohme Abrasion Test for Basalt Aggregate Concrete, Bitlis Eren Üniversitesi Fen Bilimleri Dergisi 14 (n.d.) 225–242.

[50] F. Eren, M. Keskinateş, B. Felekoğlu, K.T. Felekoğlu, Mineral Katkı İkamesinin Kalsiyum Alümina Çimentolu Harçların Taze Hal ve Zamana Bağlı Sertleşmiş Hal Özelliklerine Etkileri, Turkish Journal of Civil Engineering 34 (2023) 139–162.

[51] J. Liu, X. Chen, H. Rong, A. Yu, Y. Ming, K. Li, Effect of interface transition zone and coarse aggregate on microscopic diffusion behavior of chloride ion, Materials 15 (2022) 4171.

[52] Q. Liu, G. Feng, J. Xia, J. Yang, L. Li, Ionic transport features in concrete composites containing various shaped aggregates: a numerical study, Compos. Struct. 183 (2018) 371–380.

[53] L. Nilsson, M.H. Ngo, O.E. Gjørv, High-performance repair materials for concrete structures in the port of Gothenburg, in: Second International Conference on Concrete under Severe Conditions: Environment and Loading, 1998: pp. 1193–1198.

[54] U. Geological Survey, Mineral Commodity Summaries 2025, 2025.

[55] A. Sarabèr, R. Overhof, T. Green, J. Pels, Artificial lightweight aggregates as utilization for future ashes–A case study, Waste Management 32 (2012) 144–152.

[56] J. Go, S.N. Schiffres, A.G. Stevens, A.J. Hart, Rate limits of additive manufacturing by fused filament fabrication and guidelines for high-throughput system design, Addit. Manuf. 16 (2017) 1–11.

[57] G.D. Goh, K.K. Wong, N. Tan, H.L. Seet, M.L.S. Nai, Large-format additive manufacturing of polymers: a review of fabrication processes, materials, and design, Virtual Phys. Prototyp. 19 (2024) e2336160.

[58] D. Moreno Nieto, D. Moreno Sánchez, Design for Additive Manufacturing: Tool Review and a Case Study, Applied Sciences 11 (2021). https://doi.org/10.3390/app11041571.

[59] C.E. Duty, V. Kunc, B. Compton, B. Post, D. Erdman, R. Smith, R. Lind, P. Lloyd, L. Love, Structure and mechanical behavior of Big Area Additive Manufacturing (BAAM) materials, Rapid Prototyp. J. 23 (2017) 181–189. https://doi.org/10.1108/RPJ-12-2015-0183.

[60] P. Wu, J. Wang, X. Wang, A critical review of the use of 3-D printing in the construction industry, Autom. Constr. 68 (2016) 21–31.